

Modeling rough stenoses by an immersed-boundary method

Alexander Yakhot^{a,*}, Leopold Grinberg^b, Nikolai Nikitin^c

^a *Department of Mechanical Engineering, The Pearlstone Center for Aeronautical Engineering Studies, Ben-Gurion University of the Negev, Beersheva 84105, Israel*

^b *Department of Mechanical Engineering, Ben-Gurion University of the Negev, Beersheva 84105, Israel*

^c *Institute of Mechanics, Moscow State University, 1 Michurinski prospekt, 119899 Moscow, Russia*

Accepted 12 May 2004

Abstract

A pulsatile laminar flow of a viscous, incompressible fluid through a stenosed artery was simulated by an immersed-boundary method. The method allows the use of a simple (rectangular) computational domain in order to simulate a flow around a complex geometry obstacle with surface irregularities (roughness). The influence of the shape and the surface roughness on the flow resistance was explored. The obtained numerical results were validated by comparison with published experimental and numerical results. We show that the surface irregularities have no significant influence on the flow resistance across an obstacle for a physiological range of Reynolds numbers. Notwithstanding, an accurate representation of irregularities allows investigation of the near-wall effects of a realistic flow such as fluid recirculation. We show that a detailed study of flow patterns in the immediate vicinity of the irregular surface can be performed using the immersed boundary method.

© 2004 Elsevier Ltd. All rights reserved.

Keywords: Numerical simulation; Stenosis; Complex geometry; Immersed-boundary method

1. Introduction

Cardiovascular flows in a complex geometry, such as a stenosis in blood vessels or artificial valves and stents (a tiny metal tube used to prop open arteries after angioplasty), are commonly accompanied by separation, stagnation, recirculation and secondary vortex motion. In many cases, a blood is considered as a Newtonian fluid and computerized analysis of such flows is based on solving the Navier–Stokes equations. A natural flow through stenosed blood vessel is three-dimensional, time dependent and occurs in a very complex geometry whose shape is asymmetric and whose surface may contain rough irregularities which resemble small valleys. These irregularities make it very difficult to perform experimental and numerical simulations of such flows, although some attempts to study flows through occluded vessels have been made (Andersson et al., 2000; Back et al., 1984; Johnston and Kilpatrick, 1991). In most sophisticated investigations, a blood vessel with

a three-dimensional geometry was considered, while an irregular stenosis shape was approximated by a mathematically smooth surface. Flow recirculation and stagnation regions occur in the vicinity of vessel's surface irregularities. A flow in these regions are characterized by the so-called, long “residence times”. Analysis of recirculation regions near irregular walls is of primary biomedical interest because it is commonly accepted that near-wall residence time of blood cells is an important predictor of various pathologies.

A numerical study of the fundamental hydrodynamic effects in complex geometries is a challenging task when discretization of the Navier–Stokes equations in the vicinity of complex geometry boundaries being the most complex problem. The use of boundary-fitted, structured or unstructured grids in finite-element methods help to deal with this problem; however, the numerical algorithms implementing such grids are usually inefficient in comparison to those using simple rectangular meshes. This disadvantage is particularly pronounced for simulating non-steady incompressible flows when the Poisson equation for the pressure has to be solved at

*Corresponding author.

each time step. Iterative methods used for complex meshes have low convergence rates, especially for fine grids. On the other hand, very efficient and stable algorithms for solving Navier–Stokes equations in rectangular domains have been developed. These algorithms use fast direct methods for solving the Poisson’s equation for the pressure (Swarztrauber, 1974). These difficulties led to the development of approaches which allow formulate complex geometry flows on simple rectangular domains. These algorithms allow extend the problems that can be tackled numerically.

One approach is based on the immersed boundary (IB) method as introduced by Peskin (1971) during the early seventies. At present IB-based methods are considered to be a powerful tool for simulating complex flows. References of different immersed-boundary methods can be found in Balaras (2004), Fadlun et al. (2000), Kim et al. (2001), Moin (2002), Tseng and Ferziger (2003). In the present study, we applied a direct forcing immersed-boundary method developed in Kim et al. (2001) for simulating time-dependent flows through a stenosis with severe surface irregularities.

2. Numerical method

IB methods were originally developed to reduce simulating complex geometry flows to those defined on simple (rectangular) domains. To understand the method, consider a flow of an incompressible fluid around an obstacle Ω (S is its boundary) placed into a rectangular domain (Π). The flow is governed by the Navier–Stokes and incompressibility equations with the no-slip boundary condition on S .¹ The basic idea of IB methods is to describe a flow problem, defined in $\Pi - \Omega$, by solving the governing equations inside an entire rectangular Π without an obstacle, which allows using simple rectangular meshes. To impose the no-slip condition on an obstacle surface S (which becomes an internal surface for the rectangular domain where the problem is formulated), a source term \mathbf{f} (an artificial body force) is added to the Navier–Stokes equations as follows:

$$\frac{\partial \mathbf{u}}{\partial t} = -(\mathbf{u}\nabla)\mathbf{u} - \nabla p + \nu \nabla^2 \mathbf{u} + \mathbf{f}, \quad (1)$$

where \mathbf{u} is the velocity, p is the kinematic (divided by density) pressure, ν is the kinematic viscosity.

The peculiarity of the IB methods is that, even if the no-slip boundary condition is not imposed at the initial stage, it is gradually attained during the time-stepping computing procedure. In other words, the obstacle’s

boundary “gets built up” inside the surrounding fluid. For this reason, immersed-boundary methods are sometimes called “virtual body” methods.

Methods for introducing the artificial force in (1) are a crucial factor in IB approaches. Besides, the boundary S does not coincide with grid points of a rectangular mesh where the velocity values are computed. This means that in order to impose the no-slip boundary condition, implementation of numerical algorithms requires that the node velocity values be interpolated onto the boundary points. The performance and effectiveness of any IB method depends on both the source force (\mathbf{f}) and the computation data exchange (inter- and extrapolation) between the grid and the immersed (virtual) boundary points. In the following sections, we briefly outline the IB direct forcing approach.

2.1. Direct forcing IB approach

Fadlun et al. (2000) and Kim et al. (2001) developed the idea of “direct forcing” for implementing finite-volume methods on a staggered grid. According to the direct forcing approach, we consider the advanced-in-time governing equations (1)

$$\frac{\mathbf{u}^{l+1} - \mathbf{u}^l}{\Delta t} = \mathbf{F}_{NS}^l - \nabla p^l + \mathbf{f}^{l+1/2}, \quad (2)$$

where l denotes the time level, $\mathbf{F}_{NS} = \text{def} -(\mathbf{u}\nabla)\mathbf{u} + \nu \nabla^2 \mathbf{u}$. The different methods used for computing the convective and viscous terms of \mathbf{F}_{NS}^l in time-advancing schemes are unessential for understanding the idea of the IB method. In order to impose the no-slip condition, $\mathbf{u}^{l+1} = \mathbf{V}^{l+1}$, on the boundary (S) for the advanced time level, we have

$$\mathbf{f}^{l+1/2} = -\mathbf{F}_{NS}^l + \nabla p^l + \frac{\mathbf{V}^{l+1} - \mathbf{u}^l}{\Delta t} \quad \text{at } \mathbf{x} = \mathbf{x}_S. \quad (3)$$

The force defined by Eq. (3) is “direct” in the sense that \mathbf{V}^{l+1} is directly specified on the surface. However, direct application of Eq. (3) is impossible because the flow field \mathbf{u}^{l+1} in Eq. (2) is not divergence-free unless the pressure gradient ∇p is computed. In other words, the pressure gradient, which is included into Eq. (2), should be computed after calculating $\mathbf{f}^{l+1/2}$ but not before as it follows from Eq. (3). Both Kim et al. (2001) and Fadlun et al. (2000) suggest the following solution to this problem.

According to Kim et al. (2001), a provisional velocity field, $\tilde{\mathbf{u}}$, is computed from

$$\frac{\tilde{\mathbf{u}}^{l+1} - \mathbf{u}^l}{\Delta t} = \mathbf{F}_{NS}^l - \nabla p^l. \quad (4)$$

Let us denote by \mathbf{x}_f the nearest to the boundary surface grid points located inside the immersed body. At these points, the velocity $\tilde{\mathbf{u}} = \mathbf{u}_f$ is set by choosing \mathbf{u}_f to satisfy

¹Hereafter, the no-slip boundary condition means that the fluid velocity is equal to the obstacle velocity.

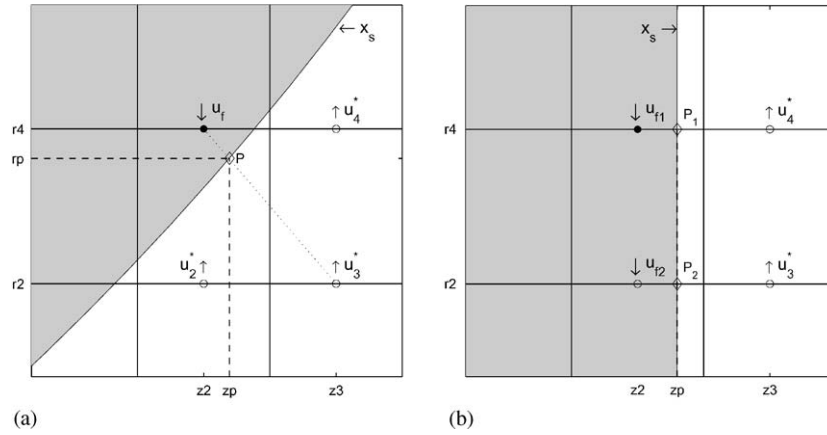


Fig. 1. (a) Bilinear and (b) linear interpolation of velocity component u_r .

the no-slip boundary condition $\tilde{\mathbf{u}} = \mathbf{V}^{l+1}$. Then, the forcing term is *explicitly* computed at these points from

$$\mathbf{f}^{l+1/2} = \frac{\mathbf{u}_f - \mathbf{u}^l}{\Delta t} - \mathbf{F}_{NS}^l + \nabla p^l \quad \text{at } \mathbf{x} = \mathbf{x}_f, \quad (5)$$

or otherwise (at $\mathbf{x} \neq \mathbf{x}_f$), $\mathbf{f}^{l+1/2} \equiv 0$.

Upon computing the source term $\mathbf{f}^{l+1/2}$, a provisional velocity field, \mathbf{u}^* , is found from

$$\frac{\mathbf{u}^* - \mathbf{u}^l}{\Delta t} = \mathbf{F}_{NS}^l - \nabla p^l + \mathbf{f}^{l+1/2}. \quad (6)$$

It is readily seen that computing the forcing term from Eqs. (4) and (5) results in satisfying the boundary condition for the provisional velocity \mathbf{u}^* .

The concept of direct forcing used in Fadlun et al. (2000) can be explained as follows. Formally, forcing is not computed from Eq. (3). In Fadlun et al. (2000), first, the provisional velocity \mathbf{u}^* is computed from Eq. (6) with $\mathbf{f}^{l+1/2} \equiv 0$. Then, at the first (nearest) to the IB grid point, but *inside the flow*, \mathbf{u}^* is re-evaluated (“corrected”) by linear interpolation of the velocity prescribed at the boundary and computed at the second grid point *inside the flow*. This procedure is equivalent to applying an artificial force.

The essential difference between the direct forcing approaches developed in Fadlun et al. (2000) and Kim et al. (2001) is that in Kim et al. (2001) forcing is applied at the grid points inside the immersed body. Secondly, different interpolation procedures are considered depending on how the immersed boundary intersects a grid cell.

In both Fadlun et al. (2000) and Kim et al. (2001), the provisional velocity field, \mathbf{u}^* satisfies the no-slip boundary condition but is not divergence-free. To impose incompressibility, \mathbf{u}^* is then projected onto a divergence-free field, \mathbf{u}^{l+1} , by the so-called pressure

correction step, viz,²

$$\frac{\mathbf{u}^{l+1} - \mathbf{u}^*}{\Delta t} = -\nabla \phi^{l+1}, \quad \nabla \cdot \mathbf{u}^{l+1} = 0. \quad (7)$$

It can be derived from (7) that the advanced pressure $p^{l+1} \approx p^l + \phi^{l+1} = p^l + O(\Delta t)$. As a result of the pressure correction step in (7), the final field, \mathbf{u}^{l+1} satisfies the incompressibility constraint, but not the no-slip boundary condition. Following Eqs. (2), (6) and (7), we obtain

$$\mathbf{u}^{l+1} = \mathbf{u}^* + O(\Delta t^2) \quad (8)$$

and, because the provisional velocity \mathbf{u}^* satisfies the no-slip boundary condition, the pressure correction step (7) changes the velocity on the immersed boundary by $O(\Delta t^2)$ at each time step. It should be noted that for steady flows the no-slip boundary condition is exactly satisfied.

2.2. IB method: numerical aspects

According to Kim et al. (2001), the procedure described in Eqs. (4)–(6) is equivalent to computing the provisional velocity \mathbf{u}^* from Eq. (6) with $\mathbf{f}^{l+1/2} \equiv 0$ followed by re-evaluating $\mathbf{u}^* = \mathbf{u}_f$ at the grid point which is nearest to the IB and located *inside* the immersed body. There are various possibilities of intersecting a computational cell by an immersed boundary. For an axisymmetric flow in cylindrical coordinates (r, z) , two such cases are shown in Fig. 1. In Fig. 1, \mathbf{u}_f is chosen so as to provide the no-slip boundary condition $\mathbf{u}^* = \mathbf{V}^{l+1}$

²In the direct forcing method developed in Kim et al. (2001), the forcing points are located on the immersed boundary or inside the body. Therefore, the cell containing the IB does not satisfy the mass conservation and a source/sink, q , must be introduced for these near-boundary cells. This means that in Eq. (7) the incompressibility constraint should be, speaking generally, written as $\nabla \cdot \mathbf{u}^{l+1} = q$. For details see Kim et al. (2001).

at the boundary *surface points* $\mathbf{x} = \mathbf{x}_S$ (point P in Fig. 1). This is achieved by interpolating the velocity values obtained at the staggered grid points of a near-boundary computational cell onto $\mathbf{x} = P$ (Fig. 1).

A linear or bilinear interpolation is used depending on the location of the near-boundary grid points. Fig. 1 illustrates an interpolating technique for the u_r velocity component. A similar procedure is applied to the u_z component. Let us consider the computational cell marked by f -2-3-4 in Fig. 1a, where the grid point marked f is located inside an “immersed body” (a shadowed area). The surface point P is located at the intersection of the boundary and the cell diagonal f -3. The velocity value u_r^* at point P is obtained using a bilinear interpolation from the surrounding grid points f -2-3-4. Thus, to impose the no-slip boundary condition at P, $u_r^*(P) \equiv V_r$, u_f is computed from

$$u_f = \frac{V_r - (1 - \alpha)\beta u_4^* - (1 - \alpha)(1 - \beta)u_3^* - \alpha(1 - \beta)u_2^*}{\alpha\beta}, \tag{9}$$

where

$$\alpha = \frac{z_3 - z_p}{z_3 - z_2}, \quad \beta = \frac{r_p - r_2}{r_4 - r_2}.$$

For the situation shown in Fig. 1b, two grid nodes (f_1 and f_2) of the computational cell (f_1 - f_2 -3-4) are located inside an immersed body. In that case, a linear interpolation is used to obtain, for example, u_{f_1} from u_4^* by substituting $\beta=1$ in Eq. (9). The value of u_{f_2} is obtained from Eq. (9) with $\beta=1$ and substituting u_4^* by u_3^* .

The IB method requires applying an interpolation procedure for the near-boundary grid points located inside the immersed body. We used a searching algorithm that enables fast identification of such points for bodies of arbitrary complex shape. The algorithm is valid for moving bodies as well. For more details on the interpolation procedure and the inner-points searching algorithm, see Grinberg (2003).

As was noted at the Section 2.1, when applying the IB method the no-slip boundary condition is exactly satisfied for steady flows. For non-steady problems, the IB method introduces an error of $O(\Delta t^2)$. To estimate this error, the L_2 -norm of the velocity components with respect to the values prescribed at the boundary points have to be monitored in time. For an axisymmetric flow with motionless boundaries, as considered in this paper, $\mathbf{V}(t, \mathbf{x}_s) = 0$ and $\mathbf{u} = (u_r, u_z)$. The L_2 -norm error in the no-slip condition for each velocity component is defined in the root-mean square form

$$L_2(w) = \sqrt{\frac{1}{N_b} \sum_{i=1}^{N_b} w_i^2}, \tag{10}$$

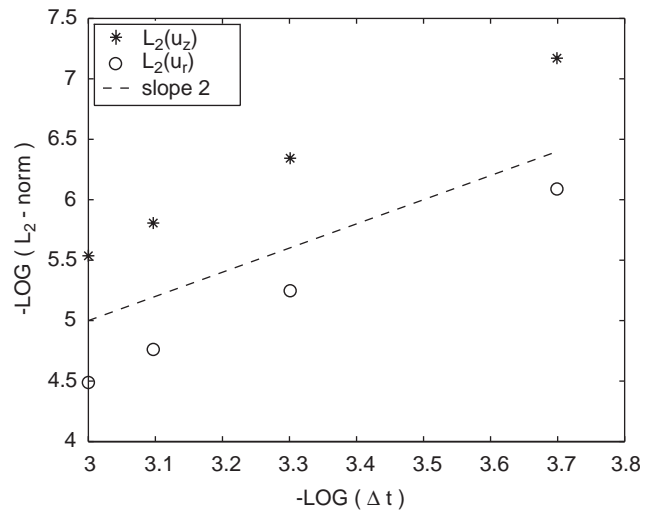


Fig. 2. L_2 -norm error for pulsatile flow, $Re_m = 40$.

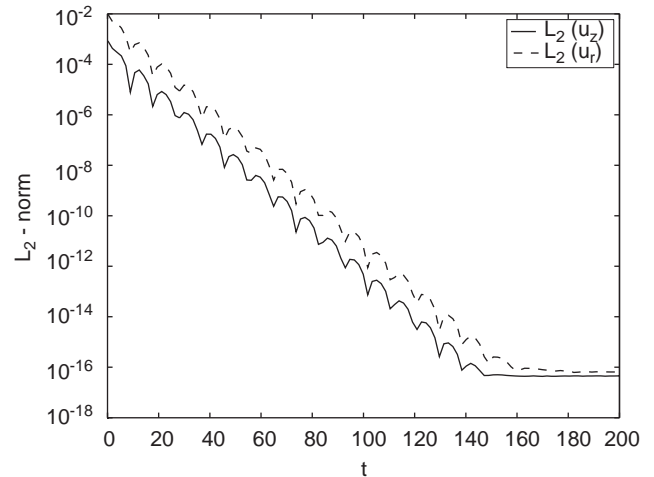


Fig. 3. L_2 -norm error for steady-state flow, $Re_m = 40$.

where $w = u_r$ or u_z and N_b is the number of selected points specifying the boundary. The results of computations can be considered reliable only if the no-slip boundary condition is satisfied with reasonable accuracy. To control the accuracy, the fluid velocity was monitored on the IB surface. Figs. 2 and 3 show the L_2 -norm error in the no-slip condition for steady and pulsatile flows through an irregular (rough) stenosis. As shown in Fig. 2, where the peak value of the L_2 -norm over the whole cycle is plotted against Δt , the direct forcing suggested by Kim et al. (2001) yields the second-order accuracy of the method. The L_2 -norm data presented in Fig. 3 for a steady-state flow show that the imposed no-slip boundary conditions are satisfied after 160 non-dimensional time units with the machine accuracy. We note that, for instance, the steady-state solution is achieved already after 30 time units because

$L_2 \approx 10^{-6}$ is enough small to conclude that the no-slip boundary condition is satisfied.

The size of the computational domain varied from 75×801 to 90×2049 in the radial and axial directions, respectively. The time step Δt is limited due to the stability constraint and in our calculations varied from $\Delta t = 0.01$ to 0.001 . The real-time consuming of steady-state simulations for one time step varied from $T_{\text{step}} = 0.2$ to 0.8 s on Pentium-IV, 2.0 GHz workstation. For the non-steady pulsatile flow simulations considered in this paper, the $L_2 \approx 4 \times 10^{-6}$ has been achieved after 15 time units. The parameters of the non-steady simulations were: 90×1025 grid, $\Delta t = 0.001$, $T_{\text{step}} = 0.33$ s. Thus, the longest run takes about 6.6 and 1.4 h for steady-state and non-steady simulations, respectively.

3. Flow through stenoses

Numerical investigation of blood flows in occluded vessels is an excellent tool for physicians in diagnosing blood vessel lesions. In early works on flow through stenoses, the stenosis shape was represented by a smooth mathematical function, such as a cosine curve. In reality, the stenosis geometry is much more complex. Usually its shape is asymmetric and the surface contains rough irregularities resembling small valleys and ridges. Back et al. (1984) published data on the geometrical contour of stenoses, which was collected from casting of a left circumflex coronary artery with mild atherosclerotic disease. This data provides a geometrical model of a rough stenosis with 48% areal occlusion. Realistic shapes of stenoses have rarely been investigated. Johnston and Kilpatrick (1991) simulated a flow through an irregular stenosis and reported excellent agreement with published experimental data for the same stenosis. When comparing the results with those of the more common smooth model, they concluded that the latter fails to predict various fluid dynamics factors, such as pressure drop, wall shear stress, recirculation regions near irregular walls, etc. Andersson et al. (2000) assessed the observation of Johnston and Kilpatrick (1991) as anomalous. To exclude the possibility that CFD predictions in Johnston and Kilpatrick (1991) were numerically inaccurate, Andersson et al. (2000) used a much higher spacial resolution for the same geometrical model of an irregular (rough) stenosis. The agreement of their results with those predicted by Johnston and Kilpatrick was excellent. However, Andersson et al. explained that Johnston and Kilpatrick's interpretation of their own results was incorrect (Andersson et al., 2000).

In their review, Berger and Jou predicted that for the future numerical simulations “the challenge to accurately model geometrically and materially complex

plaque interacting with a flowing viscous fluid will be great” (Berger and Jou, 2000). In this paper, we employ the direct forcing IB method to simulate flows through complex geometry arterial stenosis. The IB method has been applied to reproduce the stenosis geometry, including the case of a very irregular complex rough surface as provided by Back et al. (1984).

3.1. Stenosis model

Back et al. (1984) developed a numerical model of stenosis by measuring the variation of an arterial radius at 100 cross sections along the stenosis axis. The cross-sectional area of the stenosed artery was measured at intervals of $50 \mu\text{m}$ and each cross section was assumed to be a circle. A rough (irregular) stenosis profile constructed from this data is shown in Fig. 4. Hereafter, the cylindrical coordinates (r, z) are scaled with the upstream pipe's diameter, D_0 .

In the present study, we consider stenoses of three different shapes. The first is the irregular geometrical model. The second shape is the commonly used cosine curve (Andersson et al., 2000; Johnston and Kilpatrick, 1991) as expressed by

$$D(z) = D_0 - \delta \left[1 + \cos \left(\pi \frac{2z - L}{L} \right) \right], \quad 0 \leq z \leq L, \quad (11)$$

where L is the length, δ is the maximum width of the stenosis and D_0 is the upstream unoccluded diameter. The values of δ and L are set so as to obtain the same maximum area occlusion (0.48) and the same stenosis length as in the irregular model, i.e., $\delta = 0.138D_0$ and $L = 10D_0$. The third considered geometrical model is a smooth irregular model. This model has the same general geometrical shape as the irregular stenosis, but without the surface roughness elements. We note that the smooth model is no longer symmetric around its narrowest point.

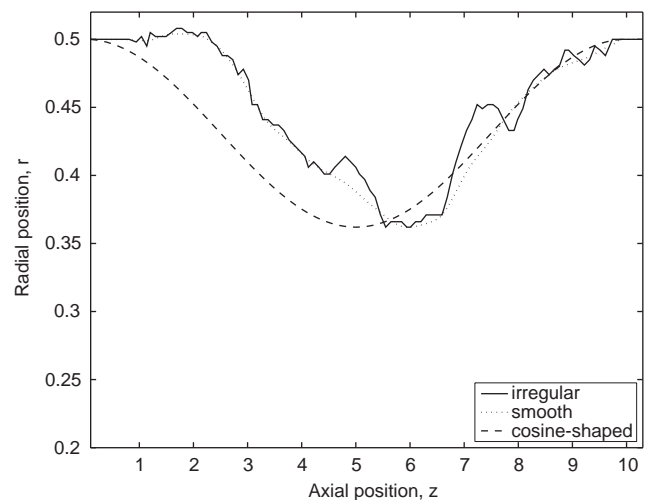
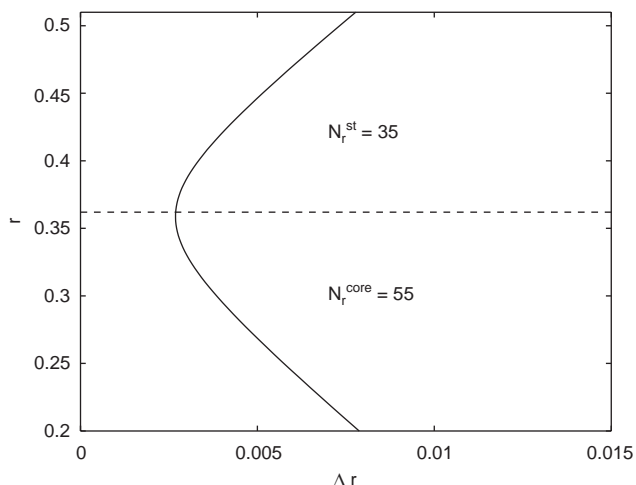
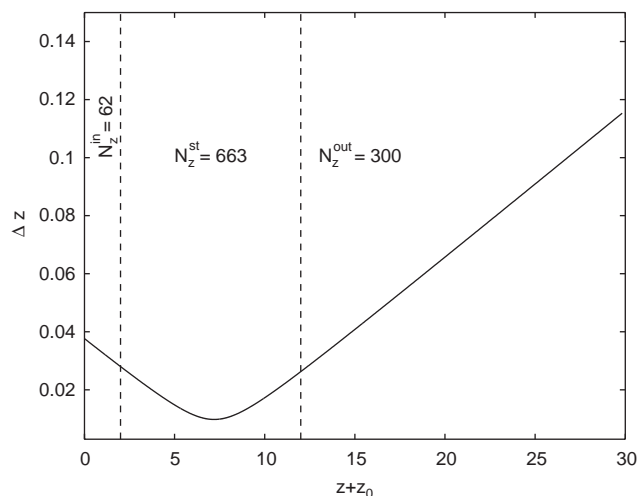
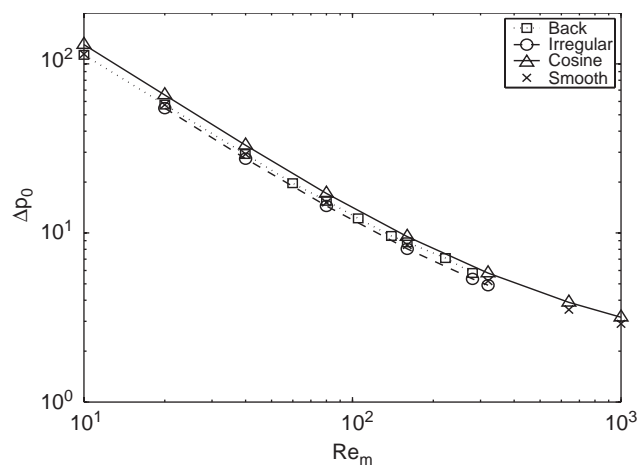


Fig. 4. Irregular, smooth and cosine-shaped stenoses.

Fig. 5. Δr spacing in radial direction.Fig. 6. Δz spacing in axial direction, $z_0 = 2$.

In this paper, we consider an axially symmetric flow of a viscous, incompressible and Newtonian fluid. For solving the governing equations, we use the standard three-level time splitting scheme with Adams–Bashforth and Crank–Nicolson discretization for the non-linear and viscous terms (e.g., see Fadlun et al., 2000). The Helmholtz equation of the viscous step and the Poisson equation of the pressure correction step were solved using the block-tridiagonal solver implementing the direct method of Swarztrauber (1974) and incorporated into the Fishpack package. The upstream pipe's diameter, D_0 , and the mean velocity, U_m , are the characteristic length and velocity, respectively, and $Re_m = U_m D_0 / \nu$ is the Reynolds number of the problem at hand. The inflow velocity profile was specified by the solution for a pulsatile flow problem in a pipe (White, 1991); the fully developed condition was imposed for the outflow. The inflow boundary conditions were specified 4–8 radii upstream from the beginning of the stenosis for low and high Reynolds numbers, respectively. The outflow boundary conditions were set 36–52 radii downstream of the end of the stenosis; the length of the stenosis is about 20 pipe radii. We employed a non-uniform mesh with grid points clustering around the stenosed area. The size of the computational domain varied from 75×801 to 90×2049 in the radial and axial directions, respectively. The Δr and Δz spacing distributions are shown in Figs. 5 and 6 for a 90×1025 grid used for the calculations (further grid refinement in the axial direction was found to be unnecessary). In Fig. 5, the distribution of Δr spacing in the r -direction is shown, where the grid points clustering in the vicinity of the stenosis' narrowest point ($r \approx 0.37$, schematically represented by a dashed line) can be seen. The grid spacing in a region of $r < 0.2$ (not shown in Fig. 5) is linearly coarsening and $\Delta r \approx 0.0127$ at $r = 0$. In Fig. 6, the

Fig. 7. Pressure drop, $\Delta p_0^c = \Delta p / (0.5 \rho U_m^2)$. Numerical (smooth, irregular, cosine) vs. experimental (Back et al., 1984) results.

stenosis is located between the dashed lines³ ($2 < z + z_0 < 12$), which corresponds to $0 < z < 10$ in Fig. 4.

In our calculations, the 100 data points provided by Back et al. (1984) to model the irregular (rough) stenosis, have been covered by $N_z^{\text{st}} = 663$ points of the computational domain along the stenosis axis.

3.2. Model validation

The stenosis models used in this study were validated by comparing the predicted pressure drop and shear stress with the experimental (Back et al., 1984) and numerical results obtained in Andersson et al. (2000),

³ Hereafter, z_0 denotes the distance between the beginning of a stenosis and the inlet upstream cross section, which means, for example, that in Fig. 10, the location $z + z_0 = 8$ corresponds to the location $z = 6$ in Fig. 4 (where the stenosis profiles are shown).

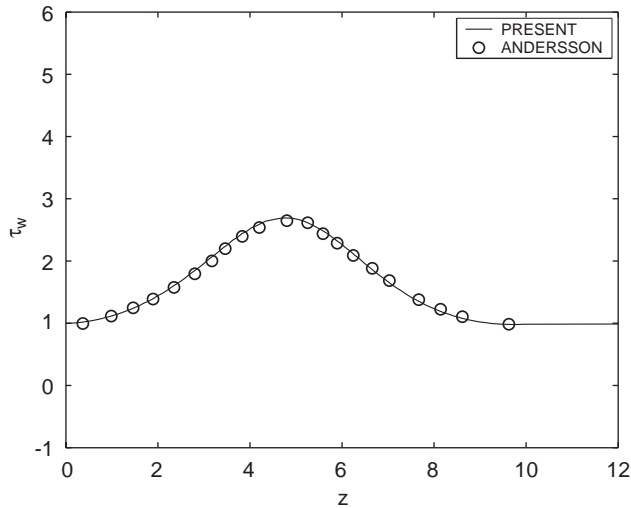


Fig. 8. Normalized wall shear stress for the cosine model, steady flow $Re_m = 20$.

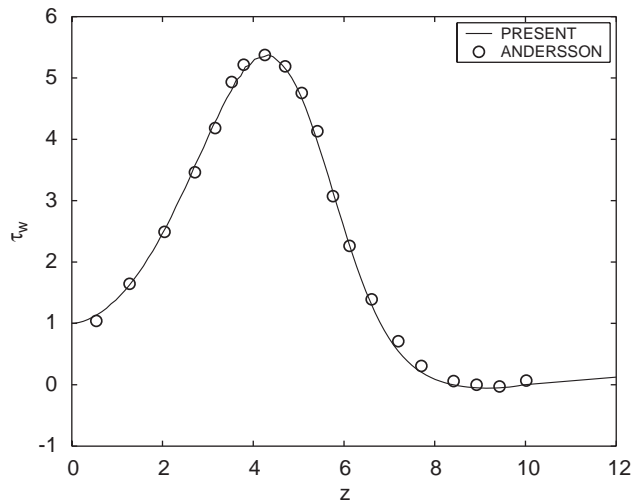


Fig. 9. Normalized wall shear stress for the cosine model, steady flow $Re_m = 1000$.

Johnston and Kilpatrick (1991). The pressure drop was computed between the axial locations at $z = 0.42$ and 10.118 from the beginning of the stenosis (Fig. 4). The numerical results obtained for three stenosis models are shown in Fig. 7, and are in excellent agreement with the experimental findings reported by Back et al. (1984) for the considered physiological flow range of Reynolds numbers, $Re_m = 100\text{--}400$. The computations for $Re > 400$ were performed to validate the suggested numerical approach by comparing the results with those reported in the literature.

Figs. 8 and 9 demonstrate the predicted wall shear stress⁴ compared with that of Andersson et al. (2000).

⁴The data is normalized by the wall shear stress in the unoccluded tube section far upstream from the stenosis.

The agreement of the results with those of Andersson et al. (2000) is excellent.

4. Smooth vs. irregular stenosis

This section presents the numerical results of simulations of flows for three geometrically different stenoses (Fig. 4). We can see from the figure that stenosis surface irregularity leads to complex flow patterns with recirculation/stagnation regions. Correct resolving of flows inside these regions is important for predicting the near-wall locations with long fluid residence times.

4.1. Pressure drop

The results of the predicted pressure drop across the stenosis is presented in Fig. 7 and are in full agreement with previous findings (Andersson et al., 2000; Johnston and Kilpatrick, 1991). The pressure drop, Δp , for the irregular and smooth stenosis geometrical models practically collapse onto the same curve, thus correlating with the experimental results of Back et al. (1984). Unsurprisingly, the pressure drop computed across the cosine-shaped stenosis shows consistently higher flow resistance: the smooth and the irregular stenosis models have almost the same sized cross-sectional area throughout the entire length of the stenosis. On the other hand, the narrower cross section of the cosine-shaped stenosis located between $z = 0$ and 6 (in Fig. 4) causes higher occlusion of the vessel and, consequently, higher flow resistance. Therefore, we agree with Andersson et al. (2000) that the pressure drop excess across the cosine-shaped stenosis (as first reported by Johnston and Kilpatrick, 1991) is a consequence of the particular geometrical shape of the stenosis and is unaffected by stenosis surface irregularities. Furthermore, while the results presented in Fig. 7 (where the pressure difference is computed along the centerline) support the conclusion drawn by Andersson et al. (2000) that the low-Reynolds number flow resistance for the irregular-shaped stenosis and its smooth model are practically indistinguishable, one can see from this figure that the longitudinal pressure drop, measured at the centerline across the smooth stenosis, is consistently higher (about 5%) than that of the irregular stenosis. We recall that the smooth stenosis model was constructed by removing the two main valleys ($z = 4\text{--}5$ and $6.5\text{--}7.5$, Fig. 4), which effectively increased the occlusion ratio. These, though minor, changes in the constriction size led to the pressure drop increase. A similar observation has been found in simulating a flow through more severe stenosis model, where the original stenosis size was doubled in the radial direction to achieve higher occlusion area (about 80%). Table 1 exhibits the terms of the balance of forces, where ΔP and ΔM are the pressure drop and

Table 1
Balance of the forces measured across the stenosis

Re_m	ΔP_{irr}	ΔM_{irr}	F_w^{irr}	ΔP_{smth}	ΔM_{smth}	F_w^{smth}
80	0.897	0.026	0.871	0.971	0.029	0.942
160	0.648	0.058	0.590	0.691	0.062	0.629
320	0.528	0.084	0.444	0.554	0.100	0.454

momentum flux computed across the stenosis ($0 < z < 10$, Fig. 4) and F_w is the friction force developed on the stenosis surface. One can see that the difference between the momentum, calculated for the irregular stenosis and its smooth model, grows as the Reynolds number increases. On the other hand, the difference between the friction force contributions decreases.

4.2. Wall shear stress

Data on wall shear stress is an important factor for the diagnostics of flows through stenosed arteries. In particular, one can expect that the wall shear stress will be directly affected by severe surface irregularities. Similar effects can be observed for flows near very rough walls containing small valleys and ridges, where each roughness element can be considered as a single cavity. Surface irregularities cause fluid trapping inside such valleys and ridges. It is worth noting that such regions correlate with the near-wall residence time for blood cells, which is a physical quantity of biomedical interest and an important predictor of pathology.

The normalized non-dimensional wall shear stress is

$$\tau_w = \left| \frac{du_s}{dn} \right|, \quad (12)$$

where s and n are the tangential and normal directions to the surface, respectively. We assume that the characteristic residence time, T_r , of a fluid in the vicinity of an irregular surface correlates with the wall shear stress and can be estimated as

$$T_r \propto \frac{1}{\tau_w}. \quad (13)$$

We computed the wall shear stress for the three geometrical models of the stenosis shape that are shown in Fig. 4. The results are presented in Figs. 10 and 11 for $Re_m = 40$ and 320, respectively. By comparing the wall shear curves presented in Figs. 10 and 11 with the stenosis surface shape (Fig. 4), we can see that the wall stress distribution along the stenosis correlates with the surface irregularities. The wall stress computed for an irregular stenosis deviates from that of the smooth one similarly to how the rough surface deviates from that of the smooth stenosis model. In Figs. 10 and 11, we can see that regions with long residence time (low τ_w) appear at $z + z_0 = 7$ and $z + z_0 = 9$. These regions correspond to the surface valleys at the same positions, $z = 5$ and 7

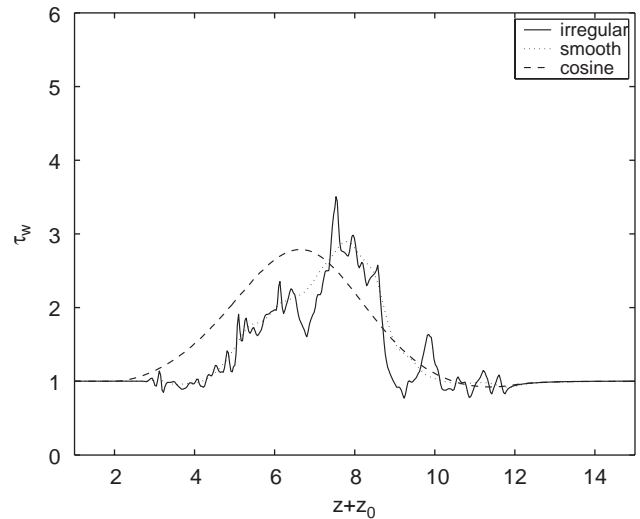


Fig. 10. Normalized wall shear stress; $Re_m = 40$, $z_0 = 2$.

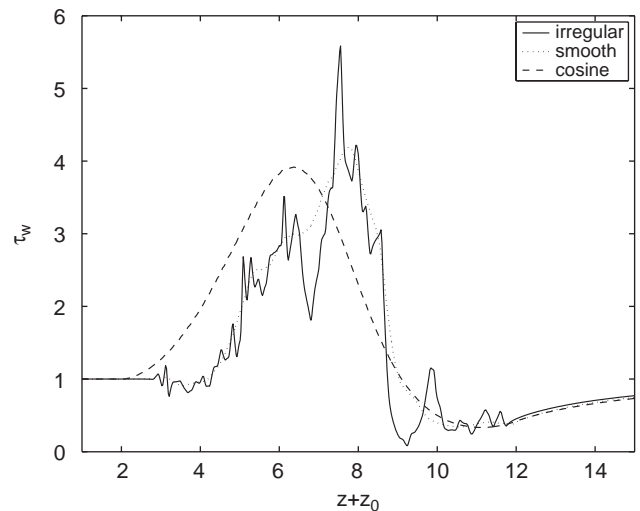


Fig. 11. Normalized wall shear stress; $Re_m = 320$, $z_0 = 2$.

(Fig. 4). To comprehend that the smooth cosine-shaped stenosis model does not exhibit any peculiar behavior of wall stress, we also show these curves in Figs. 10 and 11.

Points of flow separation are observed at those locations where the wall shear stress changes from positive to negative. The curves in Figs. 10 and 11 show no separation points. We found that the point of separation appears for flows with Reynolds numbers higher than 400 (Fig. 12). The flow separation in the vicinity of an irregular stenosis surface has been addressed by Johnston and Kilpatrick (1991). They reported a much higher Reynolds number for when flow separation is first observed, i.e., $Re^{sep} = 600$. A Reynolds number of $Re^{sep} = 400$ obtained in our calculations agrees reasonably with $Re^{sep} = 350$ as reported by Andersson (2003) for the same stenosis irregular surface. Andersson (2003) and Andersson et al. (2000) did not

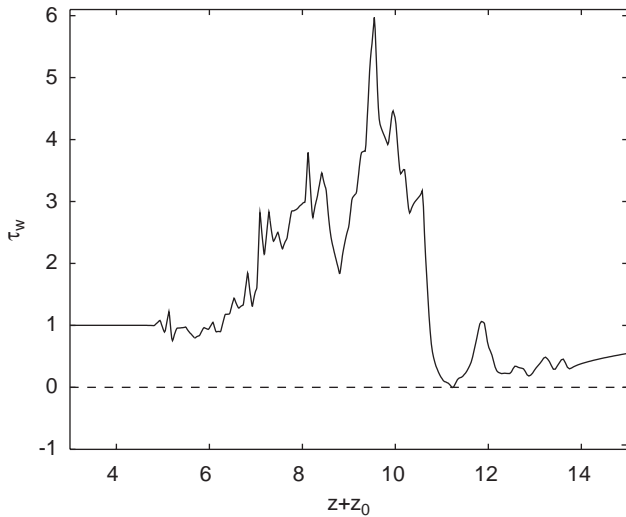


Fig. 12. Normalized wall shear stress; $Re_m = 400$, $z_0 = 4$.

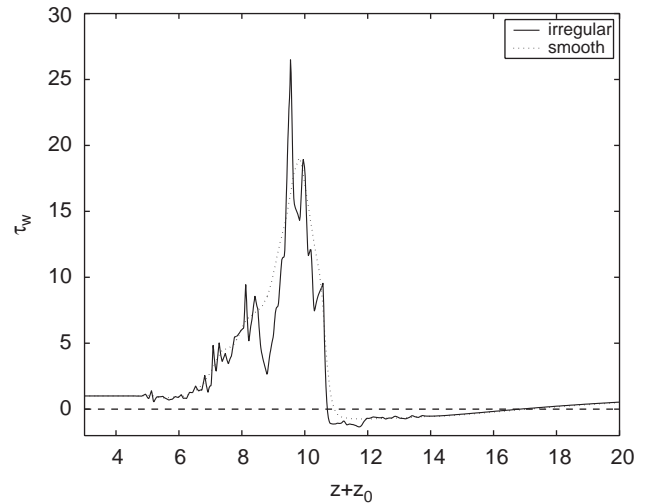


Fig. 14. Normalized wall shear stress, modified stenosis, steady flow; $Re_m = 160$, $z_0 = 4$.

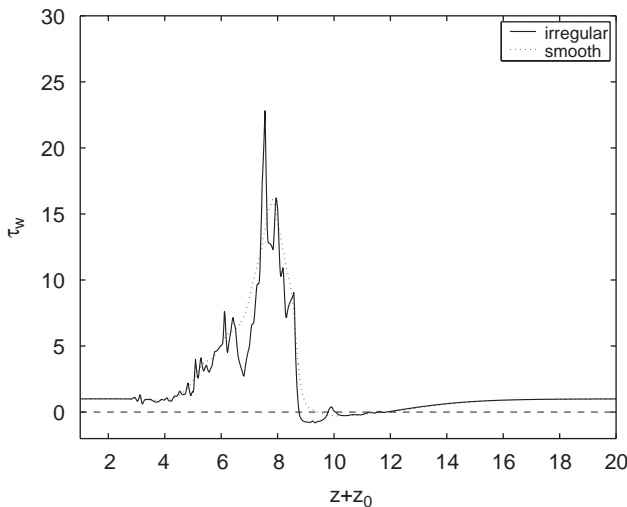


Fig. 13. Normalized wall shear stress, modified stenosis, steady flow; $Re_m = 80$, $z_0 = 2$.

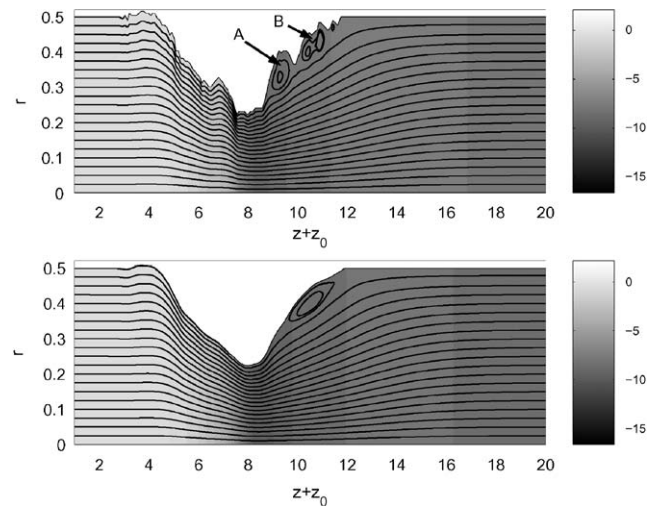


Fig. 15. Instantaneous streamlines and pressure distribution; $Re_m = 80$, $z_0 = 2$.

take into account very small irregularities reported in Back et al. (1984). In our calculations the rough stenosis geometry was exactly reproduced by the IB method. The separation Reynolds number, $Re^{sep} = 600$, in Johnston and Kilpatrick (1991) should be considered as an overestimation due to the fact that a coarse grid was used for the calculations.

Recirculation regions are commonly present in those blood vessels which tend to suffer from a high degree of occlusion. To perform a numerical investigation of recirculation phenomena, the original irregular stenosis was modified by doubling its size in the radial direction to achieve a higher areal occlusion (about 80%). Wall shear stress analysis of a flow through the modified (constricted) irregular stenosis revealed several flow separation regions. For $Re_m = 80$ (Fig. 13) there were two regions (the second being miniscule) and one big

recirculation region for $Re_m = 160$ (Fig. 14). The smooth model of the modified stenosis predicts only one separation point, obviously due to its regular shape, for both $Re_m = 80$ and 160 (Figs. 13 and 14). Nevertheless, the smooth and irregular models suggest similar reattachment points, located downstream to the stenosis end for both values. One can see that the long residence time (low τ_w) regions ($z + z_0 = 7$ and 9 in Fig. 13; $z + z_0 = 9$ and 11 in Fig. 14) correspond to the irregular stenosis surface valleys ($z = 5$ and 7, respectively, shown in Fig. 4).

In Fig. 15, the instantaneous streamlines of a flow through irregular and smooth constricted stenoses are shown for $Re_m = 80$. The background color represents the pressure distribution. It is clearly seen that recirculation regions (marked by A and B) develop in

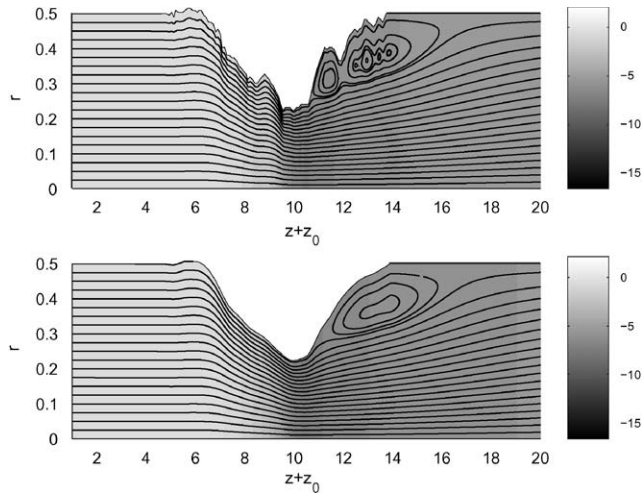


Fig. 16. Instantaneous streamlines and pressure distribution; $Re_m = 160$, $z_0 = 4$.

the two large valleys beyond the narrowest point in the diverging part of the irregular stenosis. The two neighboring vortices (A and B) co-rotate with the standard X-neutral point developing between them. This situation is unstable, and for higher Reynolds numbers may lead to merging of the two recirculation zones, A and B. Fig. 16 shows the instantaneous streamlines and pressure distribution for a flow through an irregular and smooth constricted (80%) stenosis for $Re_m = 160$. In Fig. 16, we can distinguish only one recirculation zone for both irregular and smooth stenoses. The vortex merging/breakdown, observed in the figure, can be attributed to non-linear effects which become increasingly important in flows at high Reynolds numbers. The presence of only one recirculation region can be attributed to high velocity achieved in the stenosis diverging part.

5. Pulsatile flows through rough stenoses

A realistic blood flow is pulsatile in nature. The waveform of the average axial velocity is mainly relevant for simulations, while different forms of spatially averaged inlet flow are applied to model the systole and diastole blood circulation cycles (Berger and Jou, 2000; Park, 1989). In this section, we simulate a pulsatile flow driven through a stenosis by sinusoidally time-varying pressure drop

$$\Delta p(t) = \Delta p_0 [1 + \gamma_p \sin(\omega t)], \quad (14)$$

where Δp_0 is a prescribed pressure difference across a computational domain, γ_p and $\omega = \omega_0 D_0 / 2U_m$ are, respectively, the non-dimensional amplitude and frequency of the imposed pressure drop oscillations. For the considered problem, the Womersley number,

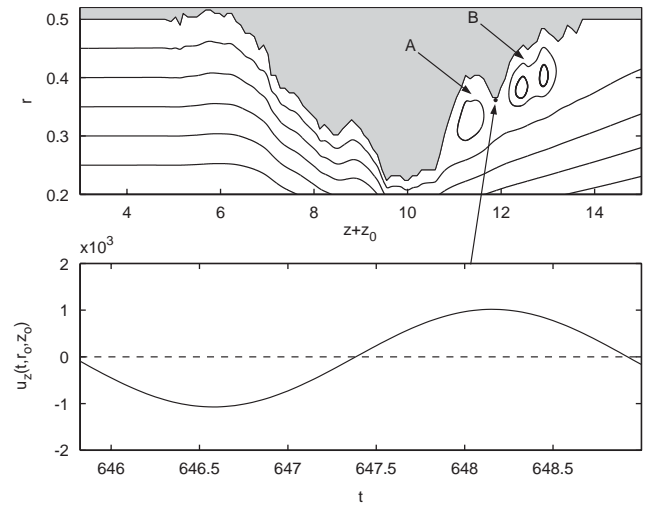


Fig. 17. Pulsatile flow, $Re_m = 100$; $Ws = 10$. Instantaneous streamlines at $t = 648.1$ and the axial velocity, u_z ; $z_0 = 4$.

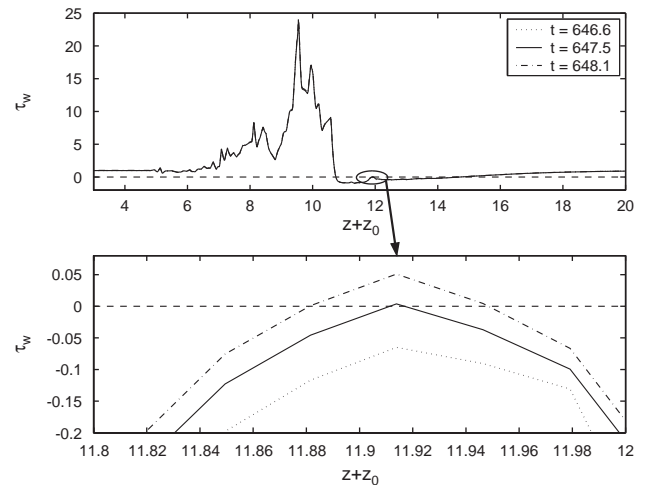


Fig. 18. Pulsatile flow, $Re_m = 100$; $Ws = 10$. Wall shear stress τ_w for different times.

$Ws = 0.5D_0(\omega_0/\nu)^{1/2}$, is a measure of the oscillating effects in a flow.⁵ The pulsatile regime here is relatively simple, but can serve as an appropriate test for simulation of a time-dependent flow in a complex geometry by the IB method.

Fig. 17 shows the instantaneous streamlines developing inside the stenosis surface valleys (A and B). First, one can see that fluid vortical structures replicate in detail the surface complex geometry, which could be considered as evidence of high spatial resolution used for computations. This figure also demonstrates the time history of the axial velocity component, u_z , measured at the nearest-to-surface grid point between the two valleys

⁵In our calculations, we use $\gamma_p = 0.2$ and the non-dimensional frequency, ω , in Eq. (14) was specified in terms of Ws and Re_m , namely, $\omega = 2Ws^2/Re_m$.

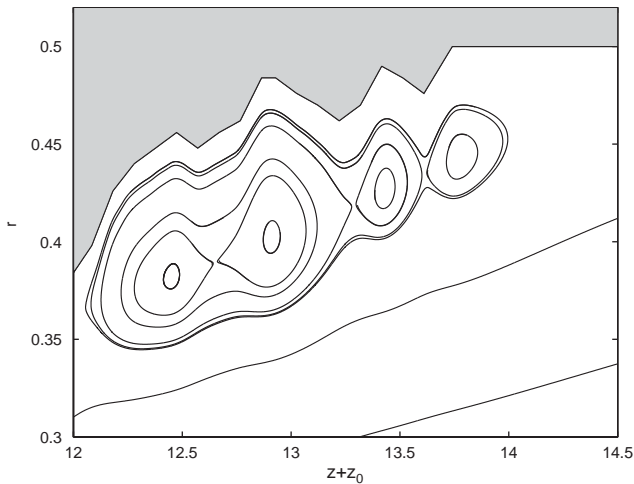


Fig. 19. Valley B: instantaneous streamlines; $Re_m = 100$, $z_0 = 4$.

and monitored throughout numerous time periods. For convenience, only one period is presented in Fig. 17. The wall shear stress, τ_w , measured in the vicinity of the stagnation point between the two valleys (around $z + z_0 = 11.9$) is presented in Fig. 18 for three different time instants. One can see that τ_w also changes the sign due to the oscillatory nature of the flow. The sign changes of the wall shear stress and the u_s —velocity indicate that the flow direction alters during the time cycle. This interesting feature deserves comment. The main flow direction is from left to right. The positive value of u_s means that two co-rotating clockwise vortices occur in the valleys A and B. On the other hand, the negative value of u_s reveals that these two vortices merge into one vortical structure. We also turn our attention to the peculiar form of the structure developed in valley B. In Fig. 19 we enlarge this region to illustrate the instantaneous streamlines which replicate the stenosis irregular shape. At the time instant shown in Fig. 19, a complex structure consists of several *co-rotating* (clockwise) vortices that are separated by “X-neutral” points. Usually the presence of the “X-neutral” points is unstable and may result in merging/breakdown of the vortices in the vicinity of a “X-neutral” point. Vortex breakdown may act as a trigger to turbulence transition downstream of the stenosis, even for moderate Reynolds numbers.

To illustrate that the surface irregularities lead to complex vortical structures in the near-wall vicinity, we show the instantaneous streamlines for the irregular and smooth stenosis in Figs. 20 and 21. The distinction between the flow patterns is obviously seen.

As already mentioned, the results obtained in the present study for a steady flow through stenosis confirmed the conclusion drawn in Andersson et al. (2000) that the resistance of a low-Reynolds number laminar flow is unaffected by stenosis surface irregular-

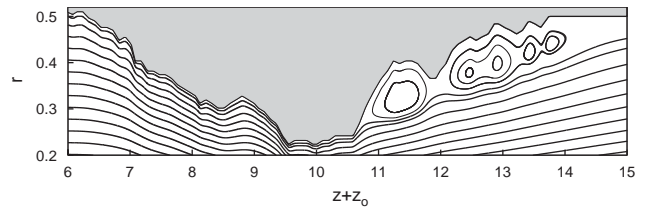


Fig. 20. Irregular model: pulsatile flow, instantaneous streamlines; $Re_m = 100$.

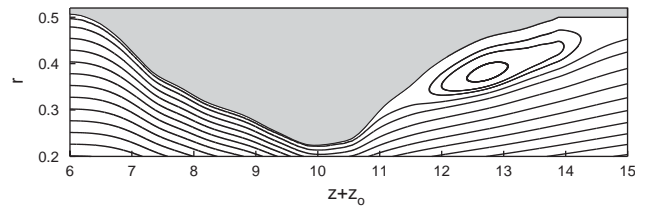


Fig. 21. Smooth model: pulsatile flow, instantaneous streamlines; $Re_m = 100$.

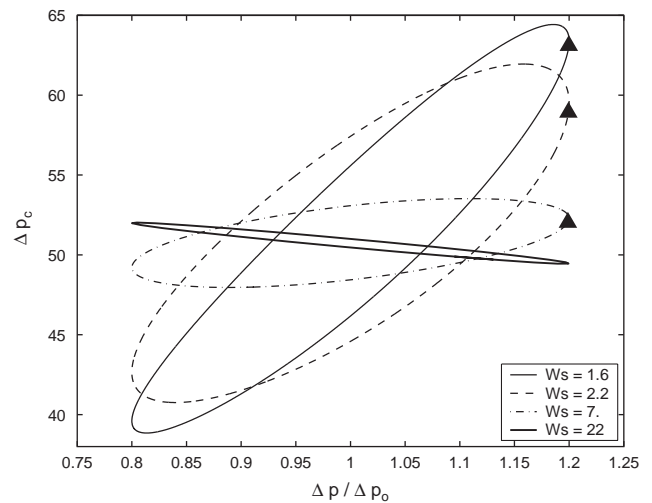


Fig. 22. Irregular stenosis, pulsatile flow, $Re_m = 100$.

rities. However, on the basis of our preliminary observations of a pulsatile flow, it would seem that modeling a realistic geometry is important because surface irregularities may affect the dynamics of the near-wall vortices. The correct prediction of the vortex dynamics might be important for estimating the near-wall residence times for blood cells. This is particularly relevant because it is now widely accepted that biological processes initiating atherosclerosis are strongly influenced by a combination of fluid and mechanical factors and occur in regions of low or oscillatory wall shear stress (Moore et al., 1999).

For a pulsatile flow around a constricted (80%) stenosis, the oscillating pressure drop, measured at the centerline across the stenosed area, Δp_c , was monitored

Table 2
Phase shift, ϕ_{ps} , $Re_m = 100$

Ws	1.6	2.2	7	22
ϕ_{pc}	0.40	0.65	0.987	2.931

in time. The phase plane curves of $\Delta p_c(t)$ vs. the $\Delta p(t)/\Delta p_0$ instantaneous states are shown in Fig. 22 for different Womersley numbers. The amplitude of Δp_c oscillations depends on the Womersley number, Ws . This amplitude decreases with increasing the imposed oscillations (higher Ws). The pressure drop, Δp_c , alters very slowly for the low-frequency imposed oscillations, indicating that $\Delta p_c(t)$ has almost no phase shift with respect to the imposed pressure gradient, $\Delta p(t)$. The regime of slow oscillations can be considered as a quasi-stationary flow. For high-frequency oscillations, the pressure drop across the stenosis may oscillate in the opposite-inphase regime (Fig. 22, $Ws = 22$).

To estimate the phase shift, ϕ_{pc} , of the induced pressure drop across the stenosis with respect to the imposed oscillations (Eq. (14)), we employed the following methodology. First, we approximate $\Delta p_c(t)$ by

$$\Delta p_c(t) \approx \Delta p_{c0}(1 + \gamma_{pc} \sin(\omega t + \phi_{pc})), \quad (15)$$

where Δp_{c0} and γ_{pc} are obtained from the calculations, the phase shift, ϕ_{pc} being the best approximation for Eq. (15). An example of the phase shift obtained for $Re_m = 100$ is given in Table 2.

Using Eqs. (14) and (15), the imposed and induced pressure drop can be recast in a non-dimensional form, viz.

$$\alpha_p(t) \stackrel{\text{def}}{=} \frac{\Delta p(t) - \Delta p_0}{\gamma_p \Delta p_0} \equiv \sin(\omega t),$$

$$\alpha_{pc}(t) \stackrel{\text{def}}{=} \frac{\Delta p_c(t) - \Delta p_{c0}}{\gamma_{pc} \Delta p_{c0}} \approx \sin(\omega t + \phi_{pc}). \quad (16)$$

For flows with low-Reynolds numbers and negligibly minor non-linear effects, the equality in Eq. (16) is exact, i.e., $\alpha_{pc}(t) = \sin(\omega t + \phi_{pc})$. As such, $\alpha_{pc}(t)$ vs. $\alpha_p(t)$ phase plane instantaneous state trajectories are ellipses (Yakhot and Grinberg, 2003). Fig. 23 shows $\alpha_{pc}(t) - \alpha_p(t)$ trajectories for the irregular stenosis and its smooth model. We note that the trajectories are counter-clockwise. Open circle curves correspond to the smooth stenosis and one can see that the surface roughness does not affect the phase shift between the imposed pressure gradient and the pressure drop across the stenosis.

For a pulsatile flow, the phase plane trajectory of two calculated flow properties is an ellipse, provided that the influence of non-linear effects on the flow characteristics is negligible (Yakhot and Grinberg, 2003). The curves in Fig. 23 are shaped as ellipses, the $Ws = 7$ curve being a perfect ellipse. The $Ws = 1.6$ curve is not (especially during the deceleration cycle), owing to fundamental differences between pulsatile flows induced by relatively

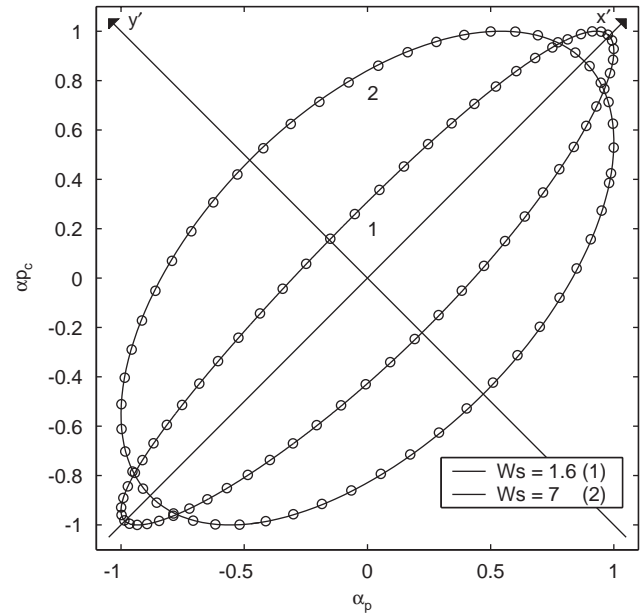


Fig. 23. $\alpha_p(t)$ vs. $\alpha_{pc}(t)$ instantaneous states for irregular and smooth stenoses, $Re_m = 100$; irregular—solid lines, smooth—open circles.

low- or high-frequency pressure gradient oscillations. Indeed, the governing equations describe the balance between the local and convective accelerations, and the viscous and pressure forces. In the case of high-frequency oscillations, when Ws is relatively large, the contribution of convective acceleration (non-linear terms) into the balance is negligible in comparison with local acceleration ($\partial \mathbf{u} / \partial t$).

6. Conclusions

We employed a direct forcing immersed-boundary method to simulate flows through complex geometry arterial stenoses. The method allows the use of a simple (rectangular) computational domain in order to simulate a flow around complex geometry obstacles. Different geometrical models of stenoses, including the case of a very irregular (rough) surface, have been considered. Our observations showed that modeling a realistic geometry is important because surface irregularities may affect the dynamics of the near-wall vortices that might be important for estimating the near-wall residence time of blood cells.

Acknowledgements

The authors wish to thank Prof. Helge Andersson for turning their attention on the irregular stenosis case and for useful comments. This research was supported by Binational United States Israel Science Foundation

Grant 2001-150 and in part by CEAR of The Hebrew University of Jerusalem. The work of NN was also supported in part by Russian Foundation for Basic Research under the Grant 02-01-00492.

References

- Andersson, H.I., 2003. Private communication.
- Andersson, H.I., Halden, R., Glomsaker, T., 2000. Effects of surface irregularities on flow resistance in differently shaped arterial stenoses. *Journal of Biomechanics* 33, 1257–1262.
- Back, L.H., Cho, Y.I., Crawford, D.W., Cuffel, R.F., 1984. Effect of mild atherosclerosis on flow resistance in coronary artery casting of man. *ASME Journal of Biomechanical Engineering* 106, 48–53.
- Balaras, E., 2004. Modeling complex boundaries using an external force field on fixed Cartesian grids in large-eddy simulations. *Computers and Fluids* 33, 375–404.
- Berger, S.A., Jou, L-D., 2000. Flows in stenotic vessels. *Annual Review of Fluid Mechanics* 32, 347–382–1262.
- Fadlun, E.A., Verzicco, R., Orlandi, P., Mohd-Yusof, J., 2000. Combined immersed-boundary finite-difference methods for three-dimensional complex flow simulations. *Journal of Computational Physics* 161, 35–66.
- Grinberg, L., 2003. Numerical simulation of a flow around stenosis. M.Sc. Thesis, Ben-Gurion University, Beersheva, Israel.
- Johnston, P.R., Kilpatrick, D., 1991. Mathematical modelling of flow through an irregular arterial stenosis. On flow resistance in coronary artery casting of man. *Journal of Biomechanics* 24, 1069–1077.
- Kim, J., Kim, D., Choi, H., 2001. An immersed-boundary finite-volume method for simulations of flow in complex geometries. *Journal of Computational Physics* 171, 132–150.
- Moin, P., 2002. Advances in large eddy simulation methodology for complex flows. *International Journal of Heat Fluid Flow* 23, 710–720.
- Moore, J.A., Steiman, D.A., Holdsworth, D.W., Ethier, C.R., 1999. Accuracy of computational hemodynamics in complex arterial geometries reconstructed from magnetic resonance imaging. *Annals of Biomedical Engineering* 27, 32–41.
- Park, D.K., 1989. A biofluid mechanics study of arterial stenoses. M.Sc. Thesis, Lehigh University, Bethlehem, PA.
- Peskin, C.S., 1971. Flow patterns around heart valves: a numerical method. *Journal of Computational Physics* 10, 252–271.
- Swarztrauber, P.N., 1974. A direct method for the discrete solutions of separable elliptic equations. *SIAM Journal of Numerical Analysis* 11, 1136–1150.
- Tseng, Yu-H., Ferziger, J., 2003. A ghost-cell immersed boundary method for flow in complex geometry. *Journal of Computational Physics* 192, 593–623.
- White, F.M., 1991. *Viscous Fluid Flow*. McGraw-Hill, New York.
- Yakhot, A., Grinberg, L., 2003. Phase shift ellipses for pulsating flows. *Physics of Fluids* 15, 2081–2083.